APPLIED SCIENCES AND ENIGINEERING

Demonstration of universal parametric entangling gates on a multi-qubit lattice

Matthew Reagor,* Christopher B. Osborn, Nikolas Tezak, Alexa Staley, Guenevere Prawiroatmodjo, Michael Scheer, Nasser Alidoust, Eyob A. Sete, Nicolas Didier, Marcus P. da Silva, Ezer Acala, Joel Angeles, Andrew Bestwick, Maxwell Block, Benjamin Bloom, Adam Bradley, Catvu Bui, Shane Caldwell, Lauren Capelluto, Rick Chilcott, Jeff Cordova, Genya Crossman, Michael Curtis, Saniya Deshpande, Tristan El Bouayadi, Daniel Girshovich, Sabrina Hong, Alex Hudson, Peter Karalekas, Kat Kuang, Michael Lenihan, Riccardo Manenti, Thomas Manning, Jayss Marshall, Yuvraj Mohan, William O'Brien, Johannes Otterbach, Alexander Papageorge, Jean-Philip Paquette, Michael Pelstring, Anthony Polloreno, Vijay Rawat, Colm A. Ryan, Russ Renzas, Nick Rubin, Damon Russel, Michael Rust, Diego Scarabelli, Michael Selvanayagam, Rodney Sinclair, Robert Smith, Mark Suska, Ting-Wai To, Mehrnoosh Vahidpour, Nagesh Vodrahalli, Tyler Whyland, Kamal Yadav, William Zeng, Chad T. Rigetti

We show that parametric coupling techniques can be used to generate selective entangling interactions for multi-qubit processors. By inducing coherent population exchange between adjacent qubits under frequency modulation, we implement a universal gate set for a linear array of four superconducting qubits. An average process fidelity of $\mathcal{F}$ = 93% is estimated for three two-qubit gates via quantum process tomography. We establish the suitability of these techniques for computation by preparing a four-qubit maximally entangled state and comparing the estimated state fidelity with the expected performance of the individual entangling gates. In addition, we prepare an eight-qubit register in all possible bitstring permutations and monitor the fidelity of a two-qubit gate across one pair of these qubits. Across all these permutations, an average fidelity of $\mathcal{F}$ = 91.6 ± 2.6% is observed. These results thus offer a path to a scalable architecture with high selectivity and low cross-talk.

INTRODUCTION

All practical quantum computing architectures must address the challenges of gate implementation at scale. Superconducting quantum processors designed with static circuit parameters can achieve high coherence times (*1*, *2*). For these schemes, however, entangling gates have come at the expense of always-on qubit-qubit couplings (*3*) and frequency crowding (*4*). Processors based on tunable superconducting qubits, meanwhile, can achieve minimal residual coupling and fast multi-qubit operations (*5*, *6*); yet, these systems must overcome flux noise decoherence (*7*, *8*) and computational basis leakage (*9*–*12*). Moreover, the difficulties faced by both fixed-frequency and tunable qubit designs are compounded as the system size grows. Parametric architectures (*13*, *14*), however, promise to overcome many of the fundamental challenges of scaling up quantum computers. By using modulation techniques akin to analog quantum processors (*15*, *16*), these schemes allow frequency-selective entangling gates between otherwise static, weakly interacting qubits.

Several proposals for parametric logic gates have been experimentally verified in the past decade. Parametric entangling gates have been demonstrated between two flux qubits via frequency modulation of an ancillary qubit (*13*, *14*), between two transmon qubits via ac Stark modulation of the computational basis (*17*) and of the noncomputational basis (*18*) with estimated gate fidelity of $\mathcal{F}$ = 81% (*18*), between two fixed-frequency transmon qubits via frequency modulation of a tunable bus resonator with $\mathcal{F}$ = 98% (*19*), between high–quality factor resonators via frequency modulation of one tunable transmon (*20*–*22*) with $\mathcal{F} = [60 \text{ to } 80]\%$ (*22*), and, finally, between a fixed-frequency and tunable transmon via frequency modulation of the same tunable transmon with $\mathcal{F}$ = 93% (*23*, *24*). Despite these significant advances, there has yet to be an experimental assessment of the feasibility of parametric architectures with a multi-qubit system.

Here, we implement universal entangling gates via parametric control on a superconducting processor with eight qubits. We leverage the results of Didier *et al.* (*23*) and Caldwell *et al.* (*24*) to show how the multiple degrees of freedom for parametric drives can be used to resolve on-chip, multi-qubit frequency-crowding issues. For a four-qubit subarray of the processor, we compare the action of parametric CZ gates to the ideal CZ gate using quantum process tomography (QPT) (*25*–*27*), estimating average gate fidelities (*28*, *29*) of $\mathcal{F}$ = 95%, 93%, and 91%. Next, we establish the scalability of parametric entanglement by comparing the performance of individual gates to the observed fidelity of a four-qubit maximally entangled state. Further, we directly quantify the effect of the remaining six qubits of the processor on the operation of a single two-qubit CZ gate. To do so, we prepare each of the 64 classical states of the ancilla qubit register and, for each preparation, conduct two-qubit QPT. Tracing out the measurement outcomes of the ancillae results in an average estimated fidelity of $\mathcal{F}$ = 91.6 ± 2.6% to the ideal process of CZ. Our error analysis suggests that scaling to larger processors through parametric modulation is readily achievable.

RESULTS

Figure 1A shows an optical image of the transmon qubit (*30*) quantum processor used in our experiment. The multi-qubit lattice consists of alternating tunable and fixed-frequency transmons, each capacitively coupled to its two nearest neighbors to form a ring topology (see

Rigetti Computing, 775 Heinz Avenue, Berkeley, CA 94710, USA.
*Corresponding author. Email: matt@rigetti.com

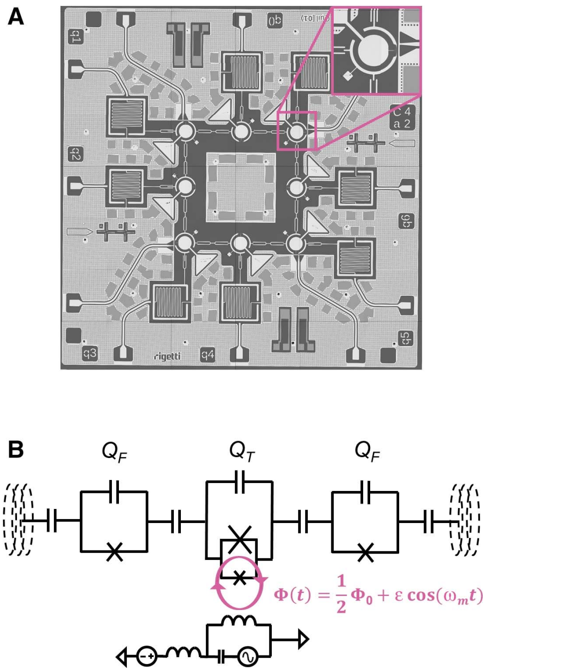

Fig. 1. Device architecture. (**A**) Optical image of the eight-qubit superconducting circuit, consisting of four fixed-frequency (Q_0, Q_2, Q_4, Q_6) and four flux-tunable transmon qubits (Q_1, Q_3, Q_5, Q_7), used in the experiments. The inset shows a zoomed-in version of one of the tunable qubits. The dimensions of the chip are 5.5 mm × 5.5 mm. (**B**) Circuit schematics of a chain of three qubits on the chip, where Q_F represents the fixed transmons and Q_T represents the tunable transmons. Each tunable qubit has a dedicated flux bias line connected to ac and dc drives combined using a bias tee, which tunes the time-dependent magnetic flux Φ(t) threaded through its asymmetric SQUID loop, as depicted by the arrows.

Materials and Methods). The Hamiltonian for a coupled tunable and fixed-frequency transmon pair is well approximated by

$$\begin{aligned}\hat{H}/\hbar = {} & 1\otimes[\omega_T(t)|1\rangle\langle 1| + (2\omega_T(t)+\eta_T)|2\rangle\langle 2|] \\ & + [\omega_F|1\rangle\langle 1| + (2\omega_F+\eta_F)|2\rangle\langle 2|]\otimes 1 \\ & + g(\sigma_1^\dagger\otimes\sigma_2 + \text{h.c.})\end{aligned} \tag{1}$$

where ω_T (ω_F) is the resonant frequency of the tunable (fixed-frequency) transmon, η_T (η_F) is the corresponding anharmonicity, g is the static capacitive coupling between the transmons, and $\sigma_i = (|0\rangle\langle 1| + \sqrt{2}|1\rangle\langle 2|)$. Modulating the flux through the SQUID loop sinusoidally results in

$$\omega_T(t) = \bar{\omega}_T + \epsilon\cos(\omega_m t + \theta_m) \tag{2}$$

where ω_m, ϵ, and θ_m are the modulation frequency, amplitude, and phase, respectively, and $\bar{\omega}_T = \omega_T + \delta\omega$ is the average frequency and accounts for a time-independent frequency shift $\delta\omega$, which leads to the interaction picture Hamiltonian (*23*, *24*)

$$\begin{aligned}\hat{H}_{\text{int}}/\hbar = \sum_{n=-\infty}^{\infty} g_n\{ & e^{i(n\omega_m-\Delta)t}|10\rangle\langle 01| \\ & + \sqrt{2}e^{i(n\omega_m-[\Delta+\eta_F])t}|20\rangle\langle 11| \\ & + \sqrt{2}e^{i(n\omega_m-[\Delta-\eta_T])t}|11\rangle\langle 02|\} \\ & + \text{h.c.}\end{aligned} \tag{3}$$

where $g_n = gJ_n(\epsilon/\omega_m)e^{i\beta_n}$ are the effective coupling strengths, $\Delta = \bar{\omega}_T - \omega_F$ is the effective detuning during modulation, $\beta_n = n(\theta_m + \pi) + \tilde{\omega}_T\sin(\theta_m/\omega_m)$ is the interaction phase, and $J_n(x)$ are Bessel functions of the first kind.

Parametric modulation of the tunable transmon's frequency is achieved by modulating the flux through the SQUID loop. As a result, $\bar{\omega}_T$ depends on the flux modulation amplitude and the dc flux bias point (*23*). Therefore, the resonance conditions for each of the terms in Eq. 3 involve both the modulation amplitude and the frequency. The first term in Eq. 3 can be used to implement an iSWAP gate (*5*, *24*, *31*) of duration $\pi/2g_n$, whereas either of the latter two terms can be used to implement a CZ gate (*9*, *10*, *24*, *32*) of duration $\pi/2g_n$. In both cases, n depends on the particular resonance condition. Although both gates are entangling and enable universal quantum computation when combined with single-qubit gates (*31*, *33*), we choose to focus on the CZ implementation to reduce phase-locking constraints on room temperature electronics. Thus, we calibrate three unique CZ gates: one between each of the neighboring pairs (Q_0,Q_1), (Q_1,Q_2), and (Q_2,Q_3).

The parametric CZ interaction between neighboring qubits can best be understood by examining the energy bands of the two-transmon subspace. Using the notation where $|ij\rangle$ corresponds to the $|i\rangle$th energy level of the fixed-frequency qubit and the $|j\rangle$th level of the tunable qubit, we show in Fig. 2A an example of the characteristic coherent oscillations that are produced as the modulation frequency of the tunable transmon is scanned through resonance with the $|11\rangle \leftrightarrow |02\rangle$ transition.

The CZ gate is activated by choosing modulation parameters that meet the resonance condition between $|11\rangle$ and $|02\rangle$ as implied in Eq. 3. This occurs when $\omega_m = (\bar{\omega}_T - \eta_T) - \omega_F$ and when the higher harmonics at $n \geq 2$ are also sufficiently detuned. Our device operates with a static flux bias of $\frac{1}{2}\Phi_0$, which makes the tunable qubit first-order insensitive to flux noise and modulation. The flux must be modulated, therefore, at a frequency of $\omega_m/2$ to meet the resonance condition for the gate (*23*). This resonance condition results in an induced coherent population exchange between the $|11\rangle$ and $|02\rangle$ energy levels of the two-transmon subspace, shown for one pair of qubits in Fig. 2 (A and B). After one cycle of oscillation in the population exchange between $|11\rangle$ and $|02\rangle$, the population of the two-photon excitation manifold returns to $|11\rangle$ (Fig. 2C) with an additional geometric phase of π, achieving the desired CZ gate (*5*).

The modulation parameters used in our parametric CZ gates are shown in Table 2. The modulation amplitude is a crucial tuning parameter for ensuring that a single interaction is activated during flux modulation, because the spectrum of induced coherent oscillations is a strong function of amplitude (see the Supplementary Materials and fig. S2). We use the static frequency shift under modulation $\delta\omega$ to calibrate the effective drive amplitude in flux quantum. The duration of the CZ gate τ is calibrated using measurements on coherent population exchange as shown in Fig. 2B, with τ being one full period of the oscillation. In Fig. 2C, two Ramsey measurements are performed on the tunable qubit: one with the fixed qubit in the $|1\rangle$ state and the other with the fixed qubit in the $|0\rangle$ state. We remove the offset phase determined in this experiment by applying $R_Z(-\theta)$ in software at compilation time to the subsequent gates on the tunable qubit, which results in approximately the ideal CZ unitary of $\hat{U}$ = diag(1, 1, 1, −1).

Next, we analyze our gates through QPT (*25*–*27*). Specifically, we characterize the behavior of each gate by reconstructing the evolution of a sufficiently large and diverse set of inputs, which corresponds to wrapping the gate by a set of pre- and post-rotations. We iterate over all pairs of rotations from the set $\hat{R}_j \in \{\hat{\mathbb{I}}, \hat{R}_x(\frac{\pi}{2}), \hat{R}_y(\frac{\pi}{2}), \hat{R}_x(\pi)\}$ acting on each qubit separately. This yields a total of 16 × 16 = 256 different experiments, each of which we repeat $N = 3000$ times. The single-shot readout data are classified into discrete positive operator-valued measure (POVM) outcomes. Assuming a multinomial model for each experiment, we can write the log-likelihood function for the full set of measurement records in terms of the histograms of POVM outcomes. This log-likelihood function is convex (*34*) in the quantum process matrix (*27*), allowing the use of the general purpose convex optimization package CVXPY (*35*) to directly solve the maximum likelihood estimation (MLE) problem (see the Supplementary Materials for more details). Imposing complete positivity (CP) and trace preservation (TP)

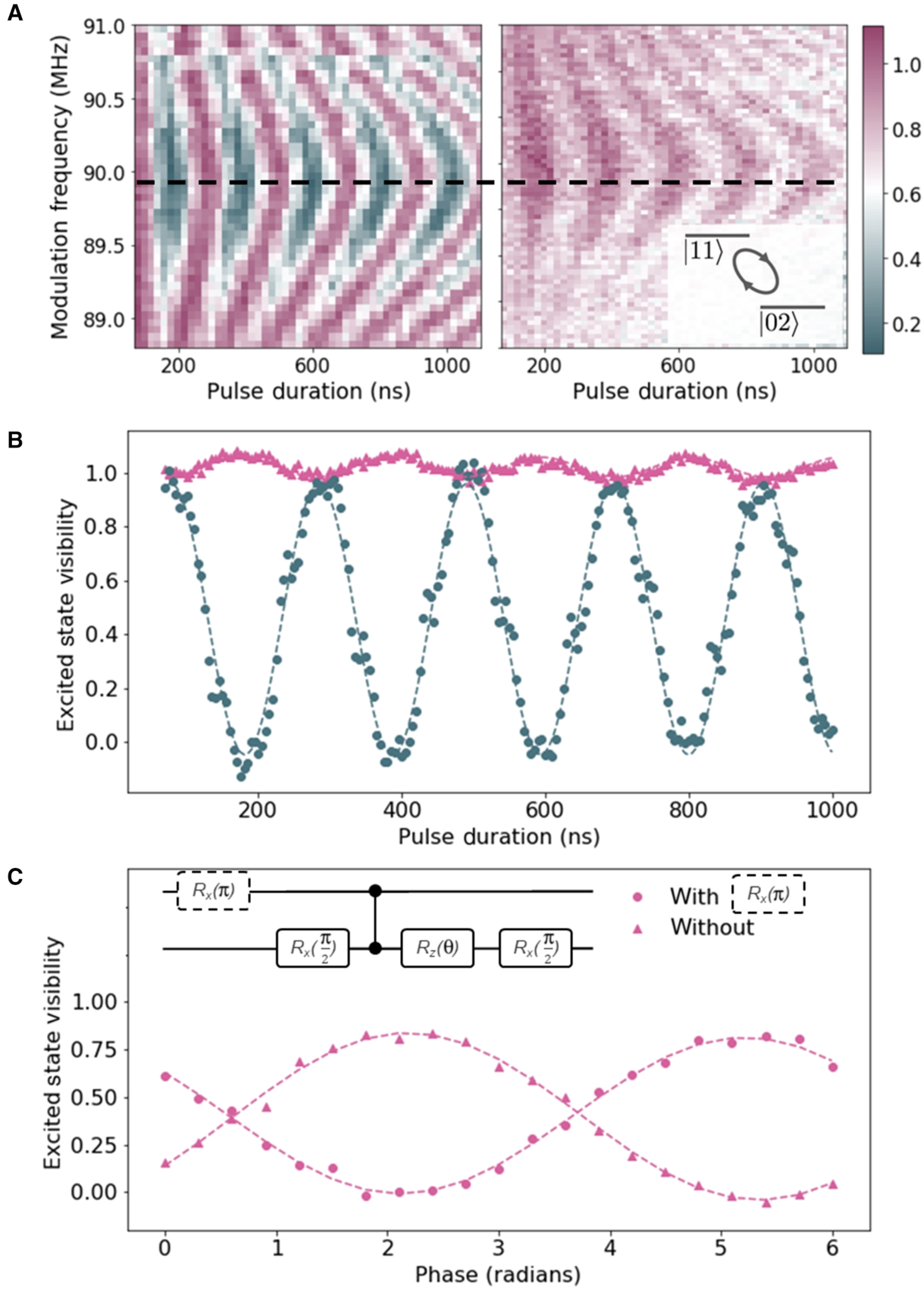

Fig. 2. Parametrically activated entangling interactions. (**A**) Under modulation, coherent population exchange is observed within the $|0\rangle \leftrightarrow |1\rangle$ subspace of Q_0 (left) and within the $|1\rangle \leftrightarrow |2\rangle$ subspace of Q_1 (right). Excited-state visibility axes are the averaged heterodyne signal of the readout pulse along an optimal *IQ* quadrature axis, scaled to the separation in the *IQ* space of the attractors associated with ground and excited states of the qubits. Inset: Energy level diagrams of the $|11\rangle \leftrightarrow |02\rangle$ transition of Q_0 and Q_1. (**B**) Data from the dashed line in (A) show the time-domain evolution between Q_0 and Q_1 on resonance, as teal (circles) and pink (triangles), respectively, allowing the identification of the target modulation duration of one period (τ = 278ns). (**C**) Determination of entangling-phase accumulation for the tunable qubit Q_1. Inset: Circuit diagram of the Ramsey interferometer used to detect a geometric phase.

constraints on the estimated process is straightforward, because CVXPY also supports general semidefinite programs. Using a basis of normalized multi-qubit Pauli operators (see the Supplementary Materials) $\{\hat{P}_k, k = 0, 1, 2, \ldots, d^2 - 1\}$, we represent a given process $\Lambda: \hat{\rho} \mapsto \Lambda(\hat{\rho})$ in terms of the Pauli transfer matrix (36) given $(\mathcal{R}_\Lambda)_{kl} := \mathrm{Tr}[\hat{P}_k \Lambda(\hat{P}_l)]$.

The Pauli transfer matrices obtained using the parametrically activated CZ gates between Q_0-Q_1, Q_1-Q_2, and Q_2-Q_3 are shown in Fig. 3 (B to D), with the ideal process matrix shown in Fig. 3A. The average gate fidelity can be computed from the Pauli transfer matrix and is given by $\mathcal{F} = \frac{d^{-1}\mathrm{Tr}\mathcal{R}^T\mathcal{R}_{\mathrm{CZ}}+1}{d+1}$, where $\mathcal{R}_{\mathrm{CZ}}$ is the Pauli transfer matrix of the ideal CZ gate. The estimates obtained from process tomography for the average gate fidelity of the CZ operations between these pairs are $\mathcal{F}$ = 95, 93, and 91%, respectively (Table 2 and Fig. 3). To within less than 1%, these results are confirmed when the MLE problem is solved under CP + TP physicality constraints.

Table 1. Characteristic parameters of the eight-qubit device. ω_r represents the frequency of the resonator, $\omega_{01}^{\max}$ is the qubit frequency (at zero flux), $\omega_{01}^{\min}$ is the frequency of the flux-tunable qubit at $\frac{1}{2}\Phi_0$, η is the anharmonicity of the qubit, T_1 is the energy relaxation time of the qubit, T_2^* is the Ramsey phase coherence time, $\mathcal{F}_{\mathrm{RO}}$ is the single-shot readout assignment fidelity, and p is the single-qubit gate average error probability estimated as the decay of polarization under randomized benchmarking with Pauli generators of the Clifford group. Note that the anharmonicities of the flux-tunable qubits are measured at their operating frequencies.

Qubit index	$\omega_r/2\pi$ (MHz)	$\omega_{01}^{\max}/2\pi$ (MHz)	$\omega_{01}^{\min}/2\pi$ (MHz)	$-\eta/2\pi$ (MHz)	T_1 (μs)	T_2^* (μs)	$\mathcal{F}_{\mathrm{RO}}$ (%)	p (%)
Q_0	5065.0	3719.1	—	216.2	34.1	18.1	95.0	1.43
Q_1	5278.0	4934.0	3817.9	204.0	17.0	4.3	93.2	0.70
Q_2	5755.0	4685.8	—	199.4	14.2	12.9	93.7	1.02
Q_3	5546.0	4870.9	3830.0	204.0	15.8	6.6	90.0	0.37
Q_4	5164.0	4031.5	—	211.0	23.7	18.7	95.2*	0.70
Q_5	5457.3	4817.6	3920.0	175.2	28.0	11.7	87.3*	2.00
Q_6	5656.8	4662.5	—	196.6	16.9	15.4	93.8*	1.20
Q_7	5388.1	4812.4	3803.5	182.8	5.6	8.6	89.9*	1.35

*Non-quantum nondemolition readout (49).

DISCUSSION

Here, we analyze the contribution of seven potential error channels to the estimated average infidelity of a single CZ gate, between (Q_1, Q_2), with $1 - \mathcal{F} = 7$ %. For each potential error source, we establish an approximate upper bound contribution to the average infidelity. We use experiments to estimate five upper bounds and perform numerical simulations to estimate the others. A summary of these results can be found in Table 3. We note that the sum of these bounds is greater than the estimated infidelity. We infer from this observation that some of these upper bounds are weak or that the effects of these errors do not combine linearly.

Decoherence mechanisms are the leading contributors to the infidelity of our gates. Operating the processor with tunable qubits statically biased to first-order insensitive flux bias points reduces the effect of flux noise on our gate set. However, coherence times are degraded during flux modulation due to the effective qubit frequency excursion from this first-order insensitive point. Furthermore, during flux modulation, the effective eigenvalues in the coupled subspace are a function of the modulation amplitude. Fluctuations in the modulation amplitude induce additional dephasing of the qubit. We measure the effective coherence time of the tunable qubits under modulation ($T_{2,\mathrm{eff}}^*$), finding

Table 2. Characteristics of the two-qubit CZ gates performed between neighboring qubit pairs (Q_0,Q_1), (Q_1,Q_2), and (Q_2,Q_3). g_n represents the effective qubit-qubit coupling under modulation, ω_m is the qubit modulation frequency, $\delta\omega$ is the tunable qubit frequency shift under modulation, τ is the duration of the CZ gate, and $\mathcal{F}_{\mathrm{QPT}}$ is the two-qubit gate fidelity measured by QPT. The theoretical tunable qubit frequency shifts under modulation ($\delta\omega^{\mathrm{th}}/2\pi$) were obtained analytically using the experimentally determined modulation frequencies ω_m and are very close to the experimentally measured values ($\delta\omega/2\pi$). The gate durations and effective qubit-qubit couplings include pulse risetimes of 40 ns to suppress the effect of pulse turn-on phase.

Qubits	$g_n/2\pi$ (MHz)	$\omega_m/2\pi$ (MHz)	$\delta\omega^{\mathrm{th}}/2\pi$ (MHz)	$\delta\omega/2\pi$ (MHz)	τ (ns)	$\mathcal{F}_{\mathrm{QPT}}$ (%)
Q_0 - Q_1	2.53	83	270	281	278	95
Q_1 - Q_2	1.83	86	323	330	353	93
Q_2 - Q_3	1.59	200	257	257	395	91

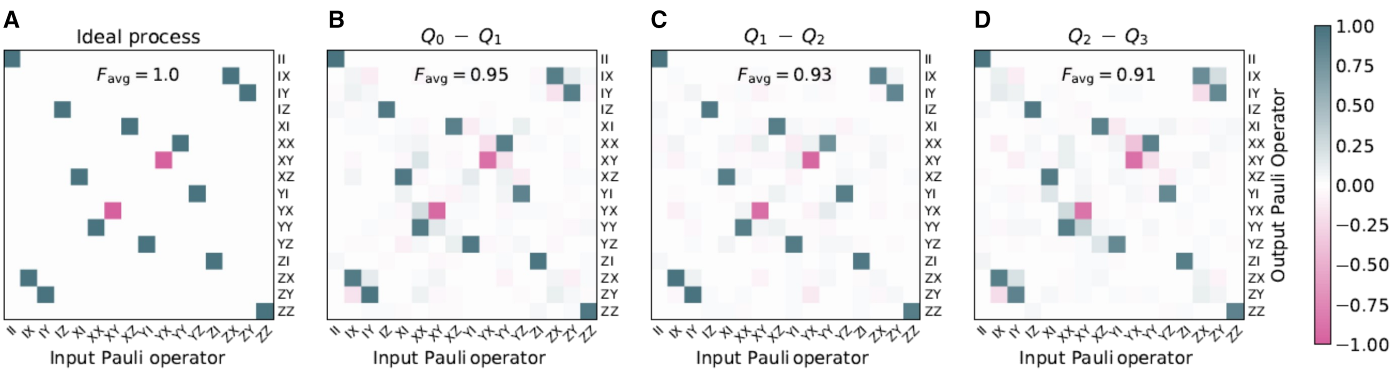

Fig. 3. Quantum process tomography. Process matrices of (**A**) the ideal process and CZ gates between (**B**) Q_0-Q_1, (**C**) Q_1-Q_2, and (**D**) Q_2-Q_3. The achieved average fidelities are measured to be 95, 93, and 91%, respectively.

Table 3. Error analysis for the two-qubit CZ gate between pairs (Q_1,Q_2). Contributions to the average infidelity estimated from QPT for several error channels.

Error channel or process	Contribution to average infidelity bound (≤%)
Decoherence	6.5
State preparation and measurement (SPAM) error	0.2
Tomography rotations	2.0
Leakage into $\|02\rangle$	6.0
Residual ZZ coupling	1.9
Spurious sidebands	0.03
Instrumentation drift	1.0

$T^{*}_{2,\mathrm{eff}} = 3 - 5.2$ μs during the parametric drives of the CZ gates (see table S1). These values are experimentally obtained by inserting a variable-time parametric drive into a Ramsey experiment. By comparing these times to the CZ gate durations, we estimate that decoherence mechanisms of the tunable qubit should dominate the infidelity of our gates at the few percentage level for the calibrated gate durations.

To more precisely estimate the effect of decoherence on the fidelity of our two-qubit gates, we follow the procedure described in equations 11 and 12 of Caldwell *et al.* (*24*). Specifically, we can estimate the unitary $\hat{V}$ that is nearest to our measured process E and calculate its fidelity against the target unitary $\hat{U}$. The infidelity between $\hat{V}$ and $\hat{U}$ is entirely due to coherent errors (because both are coherent processes) and serves as a proxy for the coherent errors of E with respect to $\hat{U}$. If $\hat{V}$ has high fidelity to $\hat{U}$, then we take that to be an indication that the contribution from coherent errors is small. In addition, if the infidelity between E and $\hat{V}$ is similar to the infidelity between E and $\hat{U}$, then we take that to be an indication that the errors are dominated by decoherence. This is precisely the behavior we observe in our two-qubit gates, and is how we determine the contribution of decoherence to the average infidelity.

We examine SPAM errors using an MLE method, which explicitly accounts for the nonideality of the readout by modeling it as a POVM that we, in turn, estimate via separate readout calibration measurements. This implies that the readout infidelity is largely accounted for and corrected by our MLE tomography. The very large number of prepared bitstrings ($d = 256$) combined with the number of repetitions per preparation ($N = 3000$) results to a statistical uncertainty of $\approx 1/\sqrt{(3000 \times 256)} \sim 0.1\%$. Even accounting for the qualitative nature of this argument, we expect the error due to an imperfectly estimated readout model to be significantly smaller than 1%.

Errors in single-qubit gates will affect the observed infidelity of a QPT experiment because these are used for pre- and post-rotations. To account for their contributions, we independently measure the infidelity of the tomography pre- and post-rotation gates via simultaneous randomized benchmarking (SRB) experiments, which are based on sequences that uniformly sample the non-entangling subgroup of the two-qubit Clifford group. A rough estimate based on the gate duration and decoherence time yields an expected infidelity of ~0.5 to 1%. The SRB experiments confirm this and yield a typical infidelity of ~1% for our tomographic pre- and post-rotations. An estimate for the resulting upper bound on the infidelity of the CZ process matrix would thus be ~1 to 2%, because there is a separate pre- and post-rotation for each QPT measurement sequence.

Because of weak anharmonicity of transmon qubits, leakage to the noncomputational subspace also contributes to the infidelity of the entangling gates. We bound leakage error by preparing the two qubits in $|11\rangle$ and applying the parametric gate. In doing so, we exit and enter the computational subspace. Imprecise control of this operation results in residual population in the transmon's second excited state. We measure this residual population in the $|2\rangle$ state to be 6% after the QPT measurement is completed. Because population out of the computational basis is unaffected by the QPT post-rotations, this population behaves as an extra decoherence channel. Bounding the resulting infidelity to the CZ gate as the full population is a worst-case approximation.

Undesired changes in the amplitude or frequency of the modulation pulse (due to instrument imperfections, temperature variations, etc.), moreover, result in an unwanted shift of the qubit effective frequency under modulation, $\bar{\omega}_T$, introducing infidelity to a QPT experiment. The effect of the former is straightforward, but the latter is a combined result of the amplitude-frequency interdependence of this modulation technique and the frequency-dependent signal transfer function through the system. This leads us to calculate

$$dF = \frac{\partial F}{\partial \bar{\omega}_T}\frac{\partial \bar{\omega}_T}{\partial t}dt \tag{4}$$

We estimate $\partial\bar{\omega}_T/\partial t$ from measurements taken over long periods of time, during which we see worst-case excursions in $\bar{\omega}_T$ of roughly 1 MHz per hour. For a full process tomography measurement, $t \sim 5$ min, resulting in a maximum frequency excursion of $\partial\bar{\omega}_T/\partial t \cdot \partial t \simeq 0.08$ MHz.

We estimate $\partial F/\partial\bar{\omega}_T$ from the linewidth of the gate's chevron pattern (Fig. 2A), which ranges from 2 to 4 MHz. Assuming a linear loss in fidelity for shifts away from the gate's frequency (chevron's center frequency), we calculate $\partial F/\partial\bar{\omega}_T \simeq 1/(2\ \mathrm{MHz})$. Hence, $\mathrm{d}F = (\partial F/\partial\bar{\omega}_T)(\partial\bar{\omega}_T/\partial t)\mathrm{d}t \simeq 0.08\ \mathrm{MHz}/2\ \mathrm{MHz} \simeq 0.04$, which provides an estimate of the contribution of undesired changes in the modulation pulse to the average infidelity. Moreover, we quantitatively estimate the last two sources of error (that is, spurious sidebands and residual ZZ coupling) using theoretical simulations after measuring the spectrum and qubit-qubit χ. The Hamiltonian expressed in the interaction picture, Eq. 3, is composed of two kinds of coupling: The always-on capacitive couplings, not specifically activated by the modulation, which correspond to the terms with $n = 0$, and spurious sidebands that correspond to $n \neq 0$. To estimate the effect of always-on coupling and spurious sidebands on the gate fidelity, we simulate the system with the relevant coupling terms separately and estimate their contributions to be ~ 1.9% and ~ 0.03%, respectively.

We benchmark the multi-qubit action of these parametric gates by running a quantum algorithm (Fig. 4) that ideally prepares a maximally entangled, four-qubit GHZ state (*6*), followed by the execution of quantum state tomography (QST) (*37*, *38*) on the resulting four-qubit state. The same set of tomography post-rotations used for QPT is also used here for QST. Similar convex optimization techniques to QPT (see the Supplementary Materials for more details) allow the tomographic inversion required to estimate the density matrix for QST. The reconstructed density matrix is shown in Fig. 4. We compute a resulting state fidelity, $\mathcal{F} = \langle\Psi|\hat{\rho}|\Psi\rangle$, to an ideal four-qubit GHZ state,

$|\Psi\rangle = (|0000\rangle + |1111\rangle)/\sqrt{2}$, of $\mathcal{F} = 79\%$. This holds both with and without the positivity $\hat{\rho} \geq 0$ constraint applied in the estimation. Assigning all the resulting state error to the action of the CZ gates results in an estimate for a geometric mean of $\mathcal{F} = 92\%$ for the three two-qubit gates, which is a difference of 0.5% from the geometric mean estimated from individual QPT analysis. We therefore conclude that further improvements to the fidelity of individual two-qubit operations will translate to improved algorithmic fidelities on this multi-qubit lattice.

To detect the coherent errors that are introduced by the effects of residual qubit-qubit coupling (with those qubits not associated with a certain two-qubit gate), we run a tomography procedure that involves all eight qubits of the processor. The circuit diagram for this measurement is shown in Fig. 5A. After first preparing all qubits in the ground state, we apply single-qubit rotations on a subregister of six ancilla qubits (Q_2-Q_7), applying either the identity gate or $R_X(\pi)$ to these qubits for a given run. Immediately thereafter, we run QPT for a CZ gate between the remaining pair of qubits (Q_0-Q_1). We repeat this procedure 64 times, once for each unique bitstring of the six-qubit register. For signal-to-noise considerations, each bitstring experiment is performed 250 times. The total experiment thus amounts to 4.1×10^6 individual measurements. The histogram of the estimated infidelities is shown in Fig. 5B. Although the mean of the distribution is $\mathcal{F} = 91.6 \pm 2.6\%$, there are a few outliers with infidelities that are larger by a statistically significant amount. Surprisingly, the worst estimated gate performance is observed for bitstrings in which one of the next-nearest-neighbor qubits (Q_3) is excited (rather than a nearest-neighbor of the pair). We attribute this error to the dispersive interaction between Q_3 and both Q_0 and Q_1: We measure these dispersive shifts to be $\delta\omega_{0,3}/2\pi = 150$ kHz and $\delta\omega_{1,3}/2\pi = 270$ kHz. For a CZ gate duration of $\tau = 278$ ns, these shifts correspond to a single-qubit phase accumulation of approximately $\delta\theta_0 = 0.26$ rad and $\delta\theta_1 = 0.47$ rad, which we associate with the observed drop in QPT fidelity. Increasing the static detuning between Q_1 and Q_3 in future designs, which is 14.5 MHz here, is expected to reduce this error channel by the squared ratio of the new detuning to the current detuning.

In addition, the estimated process fidelity versus the number of excited ancilla qubits for all measured bitstrings of the register is shown in Fig. 5C. Despite the observed variations, the average process fidelities for all but three bitstrings are within the SE of the experiment. This demonstrates that the two-qubit parametrically activated CZ gate is mostly insensitive to the ancilla qubits, compared to architectures that must directly address qubit-qubit coupling effects. This is a critical property of scalable quantum processors. It is worth noting, however, that the worst-case gate error estimates for this entangling gate should be considered for purposes such as error correction schemes.

CONCLUSION

With no need for intermediary couplers, we have demonstrated a parametric scheme for performing universal quantum computation on a four-qubit subarray of an eight-qubit processor. By doing so, we have reduced circuit design complexity and simplified the procedure to generate multi-qubit entangling gates, in a manner that is frequency-selective and alleviates the challenges of frequency crowding. We have

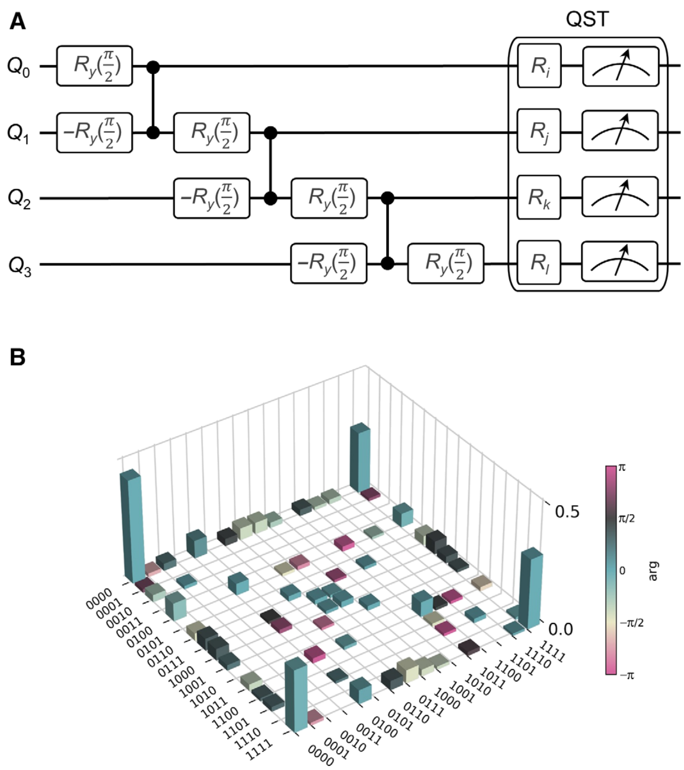

Fig. 4. QST of GHZ state. (**A**) Quantum algorithm used to prepare the state $|\Psi\rangle = (|0000\rangle + |1111\rangle)/\sqrt{2}$ using CZ gates and the QST routine used to estimate the resulting density matrix. (**B**) Reconstructed density matrix of the prepared GHZ estimated from QST. The resulting state fidelity is estimated to be $\mathcal{F} = 79\%$, in agreement with the expected performance of the three individual CZ gates, with color encoding the complex phase of each element. Density matrix elements below $|\rho_{nm}| \leq 0.01$ are cast transparent for visibility.

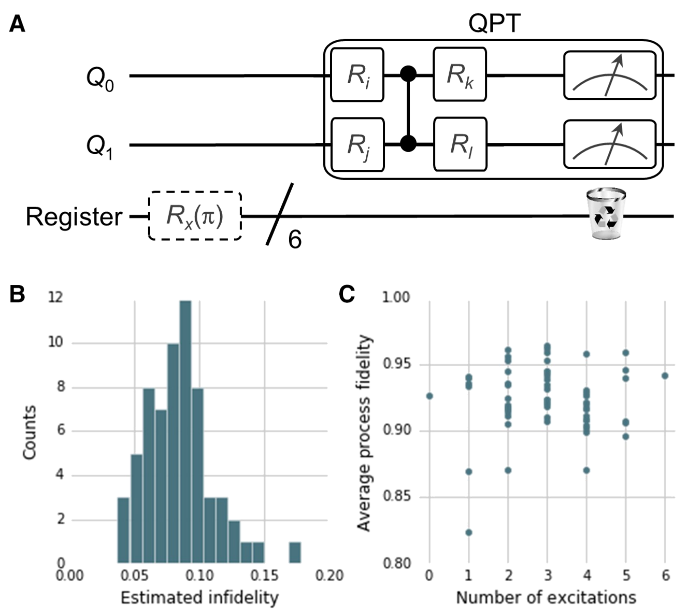

Fig. 5. Cross-talk. (**A**) Pulse sequences used for quantifying the effect of cross-talk from ancilla qubits on the performance of CZ gates. To do this, first, an arbitrary bitstring register of six ancilla qubits is prepared, with each qubit in either the ground or excited state. Then, process tomography is performed on the CZ gate between the other two qubits on the eight-qubit chip to extract a fidelity. (**B**) Histogram of the estimated infidelities measured using this algorithm. (**C**) Average process fidelities achieved as a function of the number of excited qubits in the ancilla register.

measured two-qubit gate fidelities up to 95% on the subarray and demonstrated limited sensitivity of these gates to the state of an ancilla register of the remaining six qubits. Ongoing work with this processor includes the demonstration of eight-qubit algorithms, as well as further benchmarking via multi-qubit randomized benchmarking (*39–41*) and gate-set tomography (*42–44*). Our results also highlight improvable parameters for future devices that use this architecture, which provides a promising foundation for high-fidelity, scalable quantum processors.

MATERIALS AND METHODS

The processor was fabricated on a high-resistivity silicon wafer with 28 superconducting through-silicon vias (TSVs) (*45*). These TSVs improved electromagnetic isolation and suppression of substrate modes. Our fabrication process [see the study of Vahidpour *et al.* (*45*) and the Supplementary Materials] required deep reactive-ion etching and included the deposition of superconducting material into the etched cavity. A schematic of a triplet of transmons on the chip is shown in Fig. 1B, with a flux delivery mechanism consisting of ac and dc drive sources, combined with a bias tee. The tunable transmons were designed with asymmetric Josephson junctions to provide a second flux-insensitive bias point (*21*, *30*). Characteristic parameters of all eight qubits are listed in Table 1. We observed an average energy relaxation time of $T_1 = 19.0\mu s$ and an average Ramsey phase coherence time of $T_2^* = 12.0\,\mu s$ across the chip, despite the complexity of the fabrication process. We used randomized benchmarking (*39*, *46*, *47*) to estimate the average error probabilities of the single-qubit gates at an average of $p = 1.1\%$, with the error estimated to be the decay constant of polarization for gates selected from the Pauli generators of the Clifford group. These coherence times and single-qubit gate fidelities allowed us to accurately tomograph the parametric processes in this study.

Each qubit was coupled to an individual readout resonator for low cross-talk measurements. We operated in the dispersive regime (*48*) and used individual Josephson parametric amplifiers (*16*) to amplify the readout signal. To calibrate the joint-qubit single-shot readout, we iterated over all joint-qubit basis states, preparing each state 3000 times and subsequently recording the time-averaged I and Q values of the returned signal for each qubit. By using a constant averaging filter over the demodulated returned signal, we achieved an average single-shot readout assignment fidelity of 92.3% across the chip, as listed in Table 1. Using simultaneous multi-qubit readout, we trained a separate binary classifier to predict the state of each qubit, accounting for readout cross-talk. The readout assignment fidelities quoted were defined as $\mathcal{F}_{\mathrm{RO}} := \frac{1}{2}[p(0|0) + p(1|1)]$ for each qubit. Details on readout calibration are presented in the Supplementary Materials.

SUPPLEMENTARY MATERIALS

Supplementary material for this article is available at http://advances.sciencemag.org/cgi/content/full/4/2/eaao3603/DC1
Fabrication and design
Theoretical predictions of the gate parameters
Single-shot readout
Quantum process tomography
State tomography
Process tomography
Cross-talk QPT
fig. S1. Steps of the fabrication process of the eight-qubit quantum processor.
fig. S2. Theoretical predictions for activating parametric gates between a linear chain of three qubits.
fig. S3. Raw data of readout classifier.
fig. S4. Performance of the individual trained readout classifier for a qubit.
table S1. Characteristics of the two-qubit CZ gates performed between neighboring qubit pairs (Q_0,Q_1), (Q_1,Q_2), and (Q_2,Q_3).
table S2. Averaged quantum process fidelity for different preparation states for the register of six ancilla qubits.
References (*50–55*)

REFERENCES AND NOTES

1. H. Paik, D. I. Schuster, L. S. Bishop, G. Kirchmair, G. Catelani, A. P. Sears, B. R. Johnson, M. J. Reagor, L. Frunzio, L. I. Glazman, S. M. Girvin, M. H. Devoret, R. J. Schoelkopf, Observation of high coherence in Josephson junction qubits measured in a three-dimensional circuit QED architecture. *Phys. Rev. Lett.* **107**, 240501 (2011).
2. C. Rigetti, J. M. Gambetta, S. Poletto, B. L. T. Plourde, J. M. Chow, A. D. Córcoles, J. A. Smolin, S. T. Merkel, J. R. Rozen, G. A. Keefe, M. B. Rothwell, M. B. Ketchen, M. Steffen, Superconducting qubit in a waveguide cavity with a coherence time approaching 0.1 ms. *Phys. Rev. B* **86**, 100506 (2012).
3. S. Sheldon, E. Magesan, J. M. Chow, J. M. Gambetta, Procedure for systematically tuning up cross-talk in the cross-resonance gate. *Phys. Rev. A* **93**, 060302 (2016).
4. R. Schutjens, F. A. Dagga, D. J. Egger, F. K. Wilhelm, Single-qubit gates in frequency-crowded transmon systems. *Phys. Rev. A* **88**, 052330 (2013).
5. F. W. Strauch, P. R. Johnson, A. J. Dragt, C. J. Lobb, J. R. Anderson, F. C. Wellstood, Quantum logic gates for coupled superconducting phase qubits. *Phys. Rev. Lett.* **91**, 167005 (2003).
6. R. Barends, J. Kelly, A. Megrant, A. Veitia, D. Sank, E. Jeffrey, T. C. White, J. Mutus, A. G. Fowler, B. Campbell, Y. Chen, Z. Chen, B. Chiaro, A. Dunsworth, C. Neill, P. O'Malley, P. Roushan, A. Vainsencher, J. Wenner, A. N. Korotkov, A. N. Cleland, J. M. Martinis, Superconducting quantum circuits at the surface code threshold for fault tolerance. *Nature* **508**, 500–503 (2014).
7. R. C. Bialczak, R. McDermott, M. Ansmann, M. Hofheinz, N. Katz, E. Lucero, M. Neeley, A. D. O'Connell, H. Wang, A. N. Cleland, J. M. Martinis, 1/*f* flux noise in Josephson phase qubits. *Phys. Rev. Lett.* **99**, 187006 (2007).
8. R. H. Koch, D. P. DiVincenzo, J. Clarke, Model for 1/*f* flux noise in SQUIDs and qubits. *Phys. Rev. Lett.* **98**, 267003 (2007).
9. L. DiCarlo, J. M. Chow, J. M. Gambetta, L. S. Bishop, B. R. Johnson, D. I. Schuster, J. Majer, A. Blais, L. Frunzio, S. M. Girvin, R. J. Schoelkopf, Demonstration of two-qubit algorithms with a superconducting quantum processor. *Nature* **460**, 240–244 (2009).
10. J. Ghosh, A. G. Fowler, J. M. Martinis, M. R. Geller, Understanding the effects of leakage in superconducting quantum-error-detection circuits. *Phys. Rev. A* **88**, 062329 (2013).
11. J. M. Martinis, M. R. Geller, Fast adiabatic qubit gates using only σ_z control. *Phys. Rev. A* **90**, 022307 (2014).
12. H. Ribeiro, A. Baksic, A. A. Clerk, Systematic magnus-based approach for suppressing leakage and nonadiabatic errors in quantum dynamics. *Phys. Rev. X* **7**, 011021 (2017).
13. P. Bertet, C. J. P. M. Harmans, J. E. Mooij, Parametric coupling for superconducting qubits. *Phys. Rev. B* **73**, 064512 (2006).
14. A. O. Niskanen, K. Harrabi, F. Yoshihara, Y. Nakamura, S. Lloyd, J. S. Tsai, Quantum coherent tunable coupling of superconducting qubits. *Science* **316**, 723–726 (2007).
15. E. Flurin, N. Roch, J. D. Pillet, F. Mallet, B. Huard, Superconducting quantum node for entanglement and storage of microwave radiation. *Phys. Rev. Lett.* **114**, 090503 (2015).
16. A. Roy, M. Devoret, Introduction to parametric amplification of quantum signals with Josephson circuits. *C. R. Phys.* **17**, 740–755 (2016).
17. J. Majer, J. M. Chow, J. M. Gambetta, J. Koch, B. R. Johnson, J. A. Schreier, L. Frunzio, D. I. Schuster, A. A. Houck, A. Wallraff, A. Blais, M. H. Devoret, S. M. Girvin, R. J. Schoelkopf, Coupling superconducting qubits via a cavity bus. *Nature* **449**, 443–447 (2007).
18. J. M. Chow, J. M. Gambetta, A. W. Cross, S. T. Merkel, C. Rigetti, M. Steffen, Microwave-activated conditional-phase gate for superconducting qubits. *New J. Phys.* **15**, 115012 (2013).
19. D. C. McKay, S. Filipp, A. Mezzacapo, E. Magesan, J. M. Chow, J. M. Gambetta, Universal gate for fixed-frequency qubits via a tunable bus. *Phys. Rev. Appl.* **6**, 064007 (2016).
20. F. Beaudoin, M. P. da Silva, Z. Dutton, A. Blais, First-order sidebands in circuit QED using qubit frequency modulation. *Phys. Rev. A* **86**, 022305 (2012).
21. J. D. Strand, M. Ware, F. Beaudoin, T. A. Ohki, B. R. Johnson, Alexandre Blais, B. L. T. Plourde, First-order sideband transitions with flux-driven asymmetric transmon qubits. *Phys. Rev. B* **87**, 220505 (2013).
22. R. K. Naik, N. Leung, S. Chakram, P. Groszkowski, Y. Lu, N. Earnest, D. C. McKay, J. Koch, D. I. Schuster, Random access quantum information processors. http://arxiv.org/abs/1705.00579 (2017).
23. N. Didier, E. A. Sete, M. P. da Silva, C. Rigetti, Analytical modeling of parametrically-modulated transmon qubits. http://arxiv.org/abs/1706.06566 (2017).
24. S. Caldwell, N. Didier, C. A. Ryan, E. A. Sete, A. Hudson, P. Karalekas, R. Manenti, M. Reagor, M. P. da Silva, R. Sinclair, E. Acala, N. Alidoust, J. Angeles, A. Bestwick, M. Block, B. Bloom, A. Bradley, C. Bui, L. Capelluto, R. Chilcott, J. Cordova, G. Crossman, M. Curtis, S. Deshpande, T. El Bouayadi, D. Girshovich, S. Hong, K. Kuang, M. Lenihan, T. Manning, A. Marchenkov, J. Marshall, R. Maydra, Y. Mohan, W. O'Brien, C. Osborn, J. Otterbach, A. Papageorge, J.-P. Paquette, M. Pelstring, A. Polloreno, G. Prawiroatmodjo, V. Rawat, R. Renzas, N. Rubin,

D. Russell, M. Rust, D. Scarabelli, M. Scheer, M. Selvanayagam, R. Smith, A. Staley, M. Suska, N. Tezak, D. C. Thompson, T.-W. To, M. Vahidpour, N. Vodrahalli, T. Whyland, K. Yadav, W. Zeng, C. Rigetti, Parametrically activated entangling gates using transmon qubits. http://arxiv.org/abs/1706.06562 (2017).
25. I. L. Chuang, M. A. Nielsen, Prescription for experimental determination of the dynamics of a quantum black box. *J. Mod. Opt.* **44**, 2455–2467 (1997).
26. J. F. Poyatos, J. I. Cirac, P. Zoller, Complete characterization of a quantum process: The two-bit quantum gate. *Phys. Rev. Lett.* **78**, 390–393 (1997).
27. Z. Hradil, J. Řeháček, J. Fiurášek, M. Ježek, Maximum-likelihood methods in quantum mechanics, in *Quantum State Estimation*, M. Paris, J. Řeháček, Eds. (Springer-Verlag, 2004), pp. 59–112.
28. M. Horodecki, P. Horodecki, R. Horodecki, General teleportation channel, singlet fraction, and quasidistillation. *Phys. Rev. A* **60**, 1888–1898 (1999).
29. M. A. Nielsen, A simple formula for the average gate fidelity of a quantum dynamical operation. *Phys. Lett. A* **303**, 249–252 (2002).
30. J. Koch, T. M. Yu, J. Gambetta, A. A. Houck, D. I. Schuster, J. Majer, A. Blais, M. H. Devoret, S. M. Girvin, R. J. Schoelkopf, Charge-insensitive qubit design derived from the Cooper pair box. *Phys. Rev. A* **76**, 042319 (2007).
31. N. Schuch, J. Siewert, Natural two-qubit gate for quantum computation using the XY interaction. *Phys. Rev. A* **67**, 032301 (2003).
32. J. M. Chow, J. M. Gambetta, E. Magesan, D. W. Abraham, A. W. Cross, B. R. Johnson, N. A. Masluk, C. A. Ryan, J. A. Smolin, S. J. Srinivasan, M. Steffen, Implementing a strand of a scalable fault-tolerant quantum computing fabric. *Nat. Commun.* **5**, 4015 (2014).
33. A. Barenco, C. H. Bennett, R. Cleve, D. P. DiVincenzo, N. Margolus, P. Shor, T. Sleator, J. A. Smolin, H. Weinfurter, Elementary gates for quantum computation. *Phys. Rev. A* **52**, 3457–3467 (1995).
34. S. S. Boyd, L. Vandenberghe, *Convex Optimization* (Cambridge Univ. Press, 2004).
35. S. Diamond, S. Boyd, CVXPY: A python-embedded modeling language for convex optimization. *J. Mach. Learn. Res.* **17**, 83 (2016).
36. J. M. Chow, J. M. Gambetta, A. D. Córcoles, S. T. Merkel, J. A. Smolin, C. Rigetti, S. Poletto, G. A. Keefe, M. B. Rothwell, J. R. Rozen, M. B. Ketchen, M. Steffen, Universal quantum gate set approaching fault-tolerant thresholds with superconducting qubits. *Phys. Rev. Lett.* **109**, 060501 (2012).
37. C. F. Roos, G. P. T. Lancaster, M. Riebe, H. Häffner, W. Hänsel, S. Gulde, C. Becher, J. Eschner, F. Schmidt-Kaler, R. Blatt, Bell states of atoms with ultralong lifetimes and their tomographic state analysis. *Phys. Rev. Lett.* **92**, 220402 (2004).
38. M. Steffen, M. Ansmann, R. C. Bialczak, N. Katz, E. Lucero, R. McDermott, M. Neeley, E. M. Weig, A. N. Cleland, J. M. Martinis, Measurement of the entanglement of two superconducting qubits via state tomography. *Science* **313**, 1423–1425 (2006).
39. C. A. Ryan, M. Laforest, R. Laflamme, Randomized benchmarking of single- and multi-qubit control in liquid-state NMR quantum information processing. *New J. Phys.* **11**, 013034 (2009).
40. J. P. Gaebler, A. M. Meier, T. R. Tan, R. Bowler, Y. Lin, D. Hanneke, J. D. Jost, J. P. Home, E. Knill, D. Leibfried, D. J. Wineland, Randomized benchmarking of multiqubit gates. *Phys. Rev. Lett.* **108**, 260503 (2012).
41. A. D. Córcoles, J. M. Gambetta, J. M. Chow, J. A. Smolin, M. Ware, J. Strand, B. L. T. Plourde, M. Steffen, Process verification of two-qubit quantum gates by randomized benchmarking. *Phys. Rev. A* **87**, 030301 (2013).
42. R. Blume-Kohout, J. K. Gamble, E. Nielsen, J. Mizrahi, J. D. Sterk, P. Maunz, Robust, self-consistent, closed-form tomography of quantum logic gates on a trapped ion qubit. http://arxiv.org/abs/1310.4492 (2013).
43. D. Greenbaum, Introduction to quantum gate set tomography. http://arxiv.org/abs/1509.02921 (2015).
44. R. Blume-Kohout, J. K. Gamble, E. Nielsen, K. Rudinger, J. Mizrahi, K. Fortier, P. Maunz, Demonstration of qubit operations below a rigorous fault tolerance threshold with gate set tomography. *Nat. Commun.* **8**, 14485 (2017).
45. M. Vahidpour, W. O'Brien, J. T. Whyland, J. Angeles, J. Marshall, D. Scarabelli, G. Crossman, K. Yadav, Y. Mohan, C. Bui, V. Rawat, R. Renzas, N. Vodrahalli, A. Bestwick, C. Rigetti, Superconducting through-silicon vias for quantum integrated circuits. http://arxiv.org/abs/1708.02226 (2017).
46. E. Knill, D. Leibfried, R. Reichle, J. Britton, R. B. Blakestad, J. D. Jost, C. Langer, R. Ozeri, S. Seidelin, D. J. Wineland, Randomized benchmarking of quantum gates. *Phys. Rev. A* **77**, 012307 (2008).
47. J. M. Chow, J. M. Gambetta, L. Tornberg, Jens Koch, L. S. Bishop, A. A. Houck, B. R. Johnson, L. Frunzio, S. M. Girvin, R. J. Schoelkopf, Randomized benchmarking and process tomography for gate errors in a solid-state qubit. *Phys. Rev. Lett.* **102**, 090502 (2009).
48. A. Wallraff, D. I. Schuster, A. Blais, L. Frunzio, R.-S. Huang, J. Majer, S. Kumar, S. M. Girvin, R. J. Schoelkopf, Strong coupling of a single photon to a superconducting qubit using circuit quantum electrodynamics. *Nature* **431**, 162–167 (2004).
49. M. D. Reed, L. DiCarlo, B. R. Johnson, L. Sun, D. I. Schuster, L. Frunzio, R. J. Schoelkopf, High-fidelity readout in circuit quantum electrodynamics using the Jaynes-Cummings nonlinearity. *Phys. Rev. Lett.* **105**, 173601 (2010).
50. F. Pedregosa, G. Varoquaux, A. Gramfort, V. Michel, B. Thirion, O. Grisel, M. Blondel, P. Prettenhofer, R. Weiss, V. Dubourg, J. Vanderplas, A. Passos, D. Cournapeau, M. Brucher, M. Perrot, E. Duchesna, Scikit-learn: Machine learning in Python. *J. Mach. Learn. Res.* **12**, 2825–2830 (2011).
51. G. James, D. Witten, T. Hastie, R. Tibshirani, *An Introduction to Statistical Learning: With Applications in R* (Springer, 2013).
52. M. A. Nielsen, I. L. Chuang, *Quantum Computation and Quantum Information* (Cambridge Univ. Press, 2010).
53. A. Gelman, J. Carlin, H. Stern, D. Dunson, A. Vehtari, D. Rubin, *Bayesian Data Analysis* (CRC Press, 2013).
54. E. Jeffrey, D. Sank, J. Y. Mutus, T. C. White, J. Kelly, R. Barends, Y. Chen, Z. Chen, B. Chiaro, A. Dunsworth, A. Megrant, P. J. J. O'Malley, C. Neill, P. Roushan, A. Vainsencher, J. Wenner, A. N. Cleland, J. M. Martinis, Fast accurate state measurement with superconducting qubits. *Phys. Rev. Lett.* **112**, 190504 (2014).
55. E. Magesan, J. M. Gambetta, A. D. Córcoles, J. M. Chow, Machine learning for discriminating quantum measurement trajectories and improving readout. *Phys. Rev. Lett.* **114**, 200501 (2015).

Acknowledgments: Part of this work was performed at the Stanford Nano Shared Facilities, supported by the NSF under award ECCS-1542152. **Funding:** This work was funded by Rigetti & Co Inc., dba Rigetti Computing. **Author contributions:** M. Reagor, C.B.O., N.T., A.S., G.P., M. Scheer, and N.A. designed and performed the experiments and analyzed the data. E.A.S., N.D., and M.P.d.S. proposed and performed theoretical analysis of the experimental results. M. Reagor, N.A., C.B.O., N.T., A.S., P.K., E.A.S., N.D., and M.P.d.S. performed figure planning and prepared the manuscript draft. M. Reagor and C.T.R. were responsible for the overall direction, planning, and integration among different research units. E.A., J.A., A. Bestwick, M.B., B.B., A. Bradley, C.B., S.C., L.C., R.C., J.C., G.C., M.C., S.D., T.E.B., D.G., S.H., A.H., P.K., K.K., M.L., R.M., T.M., J.M., Y.M., W.O., J.O., A. Papageorge, J.-P.P., M.P., A. Polloreno, V.R., C.A.R., R.R., N.R., D.R., M. Rust, D.S., M. Selvanayagam, R. Sinclair, R. Smith, M. Suska, T.-W.T., M.V., N.V., T.W., K.Y., and W.Z. provided hardware and software support for performing the experiments, designing and fabricating the chip, and theoretically analyzing the results. **Competing interests:** C.T.R. is the founder and chief executive officer of Rigetti & Co Inc. All authors are, have been, or may in the future be participants in incentive stock plans at Rigetti & Co Inc. E.A.S., N.D., M.P.d.S., C.T.R., M. Reagor, S.C., N.T., and C.A.R. are inventors on two pending patent applications related to this work (no. 62/521,943, filed 19 June 2017; no. 62/573,446, filed 17 October 2017). The other authors declare that they have no competing interests. **Data and materials availability:** All data needed to evaluate the conclusions in the paper are present in the paper and/or the Supplementary Materials. Additional data related to this paper may be requested from the authors.

Submitted 12 July 2017
Accepted 3 January 2018
Published 2 February 2018
10.1126/sciadv.aao3603

Citation: M. Reagor, C. B. Osborn, N. Tezak, A. Staley, G. Prawiroatmodjo, M. Scheer, N. Alidoust, E. A. Sete, N. Didier, M. P. da Silva, E. Acala, J. Angeles, A. Bestwick, M. Block, B. Bloom, A. Bradley, C. Bui, S. Caldwell, L. Capelluto, R. Chilcott, J. Cordova, G. Crossman, M. Curtis, S. Deshpande, T. El Bouayadi, D. Girshovich, S. Hong, A. Hudson, P. Karalekas, K. Kuang, M. Lenihan, R. Manenti, T. Manning, J. Marshall, Y. Mohan, W. O'Brien, J. Otterbach, A. Papageorge, J.-P. Paquette, M. Pelstring, A. Polloreno, V. Rawat, C. A. Ryan, R. Renzas, N. Rubin, D. Russel, M. Rust, D. Scarabelli, M. Selvanayagam, R. Sinclair, R. Smith, M. Suska, T.-W. To, M. Vahidpour, N. Vodrahalli, T. Whyland, K. Yadav, W. Zeng, C. T. Rigetti, Demonstration of universal parametric entangling gates on a multi-qubit lattice. *Sci. Adv.* **4**, eaao3603 (2018).